Matter-enhanced three-flavor oscillations and the solar neutrino problem

G. L. Fogli

Dipartimento di Fisica and Sezione INFN, Bari, Italy

E. Lisi

Institute for Advanced Study, Princeton, New Jersey 08540
and Dipartimento di Fisica and Sezione INFN, Bari, Italy

D. Montanino

Dipartimento di Fisica and Sezione INFN, Bari, Italy
(Received 25 March 1996)

We present a systematic analysis of the three-flavor Mikheyev-Smirnov-Wolfenstein (MSW) oscillation solutions to the solar neutrino problem, in the hypothesis that the two independent neutrino square mass differences, δm^2 and m^2, are well separated: $\delta m^2 \ll m^2$. At zeroth order in $\delta m^2/m^2$, the relevant variables for solar neutrinos are δm^2 and two mixing angles ω and ϕ. We introduce new graphical representations of the parameter space $(\delta m^2, \omega, \phi)$ that prove useful both to analyze the properties of the electron-neutrino survival probability and to present the results of the analysis of solar neutrino data. We make a detailed comparison between the theoretical predictions of the Bahcall-Pinsonneault standard solar model and the current experimental results on solar neutrino rates, and discuss thoroughly the MSW solutions found by spanning the whole three-flavor space $(\delta m^2, \omega, \phi)$. The allowed regions can be radically different from the usual "small mixing" and "large mixing" solutions, characteristic of the usual two-generation MSW approach. We also discuss the link between these results and the independent information on neutrino masses and mixings coming from accelerator and reactor oscillation searches. [S0556-2821(96)03415-7]

PACS number(s): 26.65.+t, 13.15.+g, 14.60.Pq

I. INTRODUCTION

The measurement of the $Z \to \bar{\nu}\nu$ width at the CERN Large Electron-Positron collider [1] has shown conclusively that there are three generations of light neutrinos. However, the problem as to whether the neutrinos have nonzero mass and mixing, as is the case for quarks, remains one of the most prominent experimental and theoretical problems in particle physics.

On the one hand, there is a vast and variegated set of experimental information, ranging from the negative results of laboratory neutrino oscillation searches at accelerators and reactors, to the possible indications for flavor transition processes in natural beams such as solar and atmospheric neutrinos. On the other hand, current theoretical models (e.g., the seesaw mechanism [2]) allow many different textures for the three-generation neutrino mass matrix. Thus, it seems appropriate, at this stage, to keep to a minimum the number of *a priori* assumptions in the interpretation of the experimental results.

In this work, we focus on the three-flavor Mikheyev-Smirnov-Wolfenstein (MSW) [3] neutrino oscillation solutions to the solar neutrino problem [4]. The only hypothesis that we make is to assume a neutrino mass spectrum as in Fig. 1. More precisely, we assume one of the two independent square mass differences, m^2, to be very large (more than 1 order of magnitude higher) as compared to the smallest one, δm^2, which drives the matter-enhanced oscillations.

At zeroth order in $\delta m^2/m^2$, the relevant MSW parameters (see Sec. III) are δm^2 and two mixing angles, ω and ϕ, ranging in the first quadrant $[0, \pi/2]$. We introduce new

graphical representations of the parameter space $(\delta m^2, \omega, \phi)$, that prove useful in analyzing the properties of the three-flavor MSW probability, as well as in showing the detailed results of fits to the experimental data. The parameter space is studied exhaustively, and all the solutions are

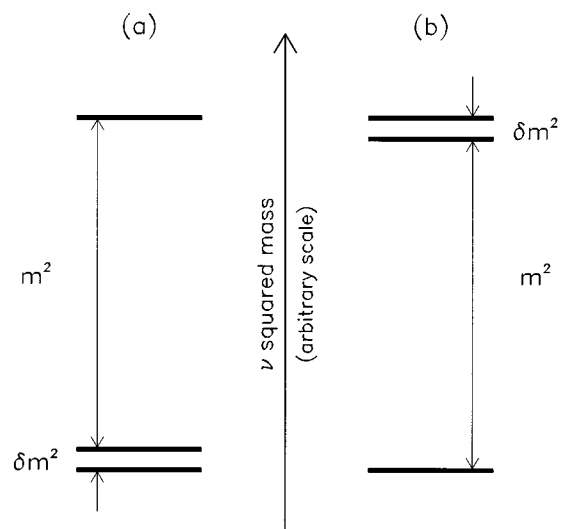ν mass spectrum hypothesis: $\delta m^2 \ll m^2$

FIG. 1. The neutrino mass spectrum assumed in this work. The hypothesis $\delta m^2 \ll m^2$ is independent of the zero of the absolute mass scale. Solar neutrinos do not distinguish the two cases (a) and (b) at zeroth order in $\delta m^2/m^2$.

TABLE I. Neutrino rates observed in the four operating solar neutrino experiments [15–18], and corresponding theoretical predictions of the standard solar model (SSM) by Bahcall and Pinsonneault [19].

Experiment	Ref.	Measured rate $\pm$ (stat)$\pm$ (syst)	Units	SSM rate [19]
Homestake	[15]	$2.55\pm0.17\pm0.18$	SNU	$9.3^{+1.2}_{-1.4}$
GALLEX	[16]	$77.1\pm8.5^{+4.4}_{-5.4}$	SNU	137^{+8}_{-7}
SAGE	[17]	$69\pm11^{+5}_{-7}$	SNU	137^{+8}_{-7}
Kamiokande	[18]	$2.89\pm0.22\pm0.35$	10^6 cm^{-2} s^{-1}	$6.62^{+0.93}_{-1.13}$

discussed thoroughly. We find three-flavor solutions to the solar neutrino problem that are considerably different from the usual two-flavor results.

The present study is more complete and detailed than previous three-flavor phenomenological analyses of the solar neutrino problem performed by other authors [5–9] and by ourselves [10–12]. The work presented in this paper is part of a wider research program, in which we intend to analyze the world neutrino oscillation data under the sole hypothesis represented by the spectrum in Fig. 1. The analysis of the most constraining accelerator and reactor experiments has already been completed [13]. We discuss the link between the information obtained in the present work from solar neutrinos and the results obtained in [13] from laboratory oscillation searches. Concerning atmospheric neutrinos, a complete three-flavor analysis (partially addressed in [10–14]) is in progress.

This paper has the following structure. In Sec. II we review the current theoretical expectations and experimental observations of the solar neutrino fluxes, and show for completeness the usual two-generation MSW fits to the data. In Sec. III we present the three-flavor oscillation formalism and show the new graphical representations of the parameter space. The properties of the ν_e survival probability are also discussed. In Sec. IV we explore the parameter space exhaustively, and find the three-flavor solutions to the solar neutrino problem. Both in Sec. III and in Sec. IV we show how solar neutrino results can be compared to the information coming from accelerator and reactor neutrino experiments. We conclude and summarize our work in Sec. V.

II. SOLAR NEUTRINO PROBLEM AND TWO-GENERATION MSW SOLUTIONS

In this section we present the experimental data used in this work, and compare them with the theoretical expectations. Particular attention is paid to correlation effects. Although our paper is focused on the three-flavor MSW mechanism, we also show, for the sake of completeness, our fit to the data in the simpler and more familiar two-generation approach.

A. Experimental data and theoretical predictions

There are four operating solar neutrino experiments: The Homestake [15] chlorine (Cl) detector, the GALLEX [16] and SAGE [17] gallium (Ga) detectors, and the Kamiokande [18] water-Cherenkov detector. The observed solar neutrino rates are shown in Table I, along with the corresponding theoretical values as predicted in the recent refined standard solar model (SSM) by Bahcall and Pinsonneault (BP) [19].

The significant deficit of observed neutrinos constitutes the well-known ''solar neutrino problem'' [4].

The information contained in Table I does not characterize completely the significance of the solar neutrino problem, since the theoretical uncertainties (last column of Table I) are not independent. It has been shown in a previous work [20] that the correlation of the uncertainties can be calculated analytically, starting from the errors affecting the SSM input parameters and the neutrino capture cross sections.

In Fig. 2 we show the experimental and theoretical 99% C.L. contours ($\Delta\chi^2=9.21$, $N_{DF}=2$) for any couple of experiments (the GALLEX and SAGE data have been combined quadratically). The projections of the ellipses onto the coordinate axes represent, with good approximation, the $\pm3\sigma$ errors for each experiment separately. Notice the strong correlation of the theoretical errors. If the correlations were neglected, the theoretically allowed regions would be larger and the discrepancy with the experiments would be underestimated [20–23].

The last relevant piece of data is the night-day ($N-D$) asymmetry of the solar neutrino flux as measured in the Kamiokande detector [24,18]:
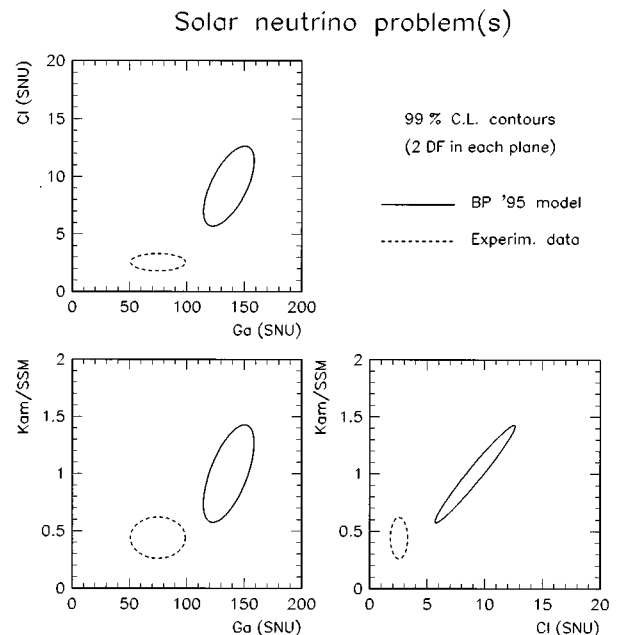

FIG. 2. The regions allowed at 99% C.L. by the present solar neutrino data (dashed lines) and by the standard solar model (SSM) of Bahcall-Pinsonneault [19] (solid lines). The coordinates are the chlorine (Cl), gallium (Ga), and water-Cherenkov (normalized Kam/SSM) signals.

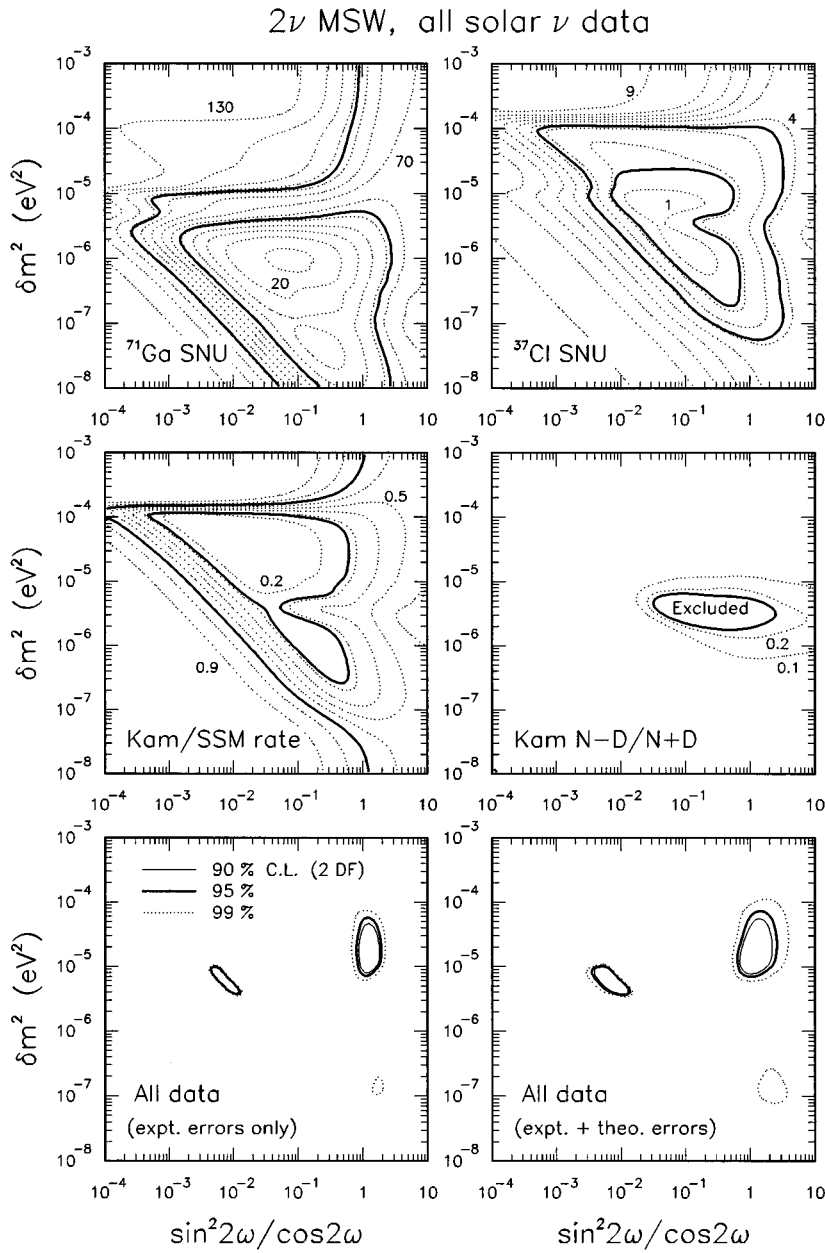## 2ν MSW, all solar ν data

FIG. 3. Two-generation MSW solutions to the solar neutrino problem. In the upper four panels (fits to single data), the solid lines define the regions allowed at 95% C.L. for two degrees of freedom (including theoretical errors), and the dotted lines represent isosignal contours. In the lower two panels (fits to all data), the MSW solutions are shown at 90%, 95%, and 99% C.L., without and with theoretical errors.

$$\frac{N-D}{N+D} = 0.07 \pm 0.07(\text{stat}) \pm 0.04(\text{syst}). \qquad (1)$$

The above value is consistent with no asymmetry (i.e., no oscillations), and thus contributes to exclude a part of the neutrino oscillation parameter space.

B. Two-generation MSW analysis

The MSW mechanism [3] of matter-enhanced neutrino oscillations is one of the most promising candidates for the solution of the solar neutrino problem (for reviews, see [25–28]). In the hypothesis that only two neutrino generations are involved in the ν_e transitions, the relevant parameters are one mass square difference, δm^2, and one mixing angle, ω.

Even in the simple two-family scenario, the calculation of the electron neutrino survival probability, $P(\nu_e \to \nu_e)$, as well as the data analysis, are not trivial tasks and require refined computer codes. We take this opportunity to mention

a few state-of-the-art features of our codes. We smear $P(\nu_e \to \nu_e)$ over the neutrino production region in the most general way, i.e., we also consider neutrino production points off the line that joins the center of the sun and the detector. This requires a double (radial and azimuthal) space integration in the sun, as well as the evaluation of the solar electron density gradient along off-radial trajectories (instead of the simple derivative). The possibility of a double resonance (see, e.g., [27,29]) is included. We also include the (computer time-consuming) earth regeneration effect [30] at each detector location, and in particular we calculate the night-day asymmetry [31] at the Kamiokande site. The earth electron density is modeled as a step function with five steps [10], corresponding to the relevant radial shells [32]. The theoretical uncertainties and their correlation effects are taken into account in the statistical χ^2 analysis of the data [20].

The results of our two-flavor analysis are shown in Fig. 3. The thick, solid lines represent the contours of the regions

allowed at 95% C.L. ($\Delta\chi^2 = 5.99$, $N_{DF} = 2$). In the first four panels, dotted lines represent curves of isosignal. In the last two panels, all data are combined without and with theoretical errors, and the allowed regions at 90%, 95%, and 99% C.L. are shown. Notice the widening of the ''small'' and ''large'' mixing angle solutions when the theoretical uncertainties are taken into account. A third solution appears at 99% C.L. for large angles and small δm^2.

When all the uncertainties are included, the χ^2 function reaches its minimum, $\chi^2_{\min} = 0.74$, at $\sin^2 2\omega = 8.06 \times 10^{-3}$ and $\delta m^2 = 5.21 \times 10^{-6}$ eV^2. The secondary (large angle) minimum is reached at $\sin^2 2\omega = 0.64$ and $\delta m^2 = 1.45 \times 10^{-5}$ eV^2, with a value $\chi^{2\prime}_{\min} = 1.89$—not a bad fit.

The MSW solutions in Fig. 3 compare well with the most recent two-generation analyses of the solar neutrino problem [22,23,33–38], modulo small differences due to the input data and their treatment. In particular, we have verified that, excluding the earth regeneration effect, our results become very similar to those obtained very recently by Bahcall and Krastev in [38], where the same solar model and experimental data were used as input.

III. THREE-FLAVOR MSW SOLAR NEUTRINO OSCILLATIONS: THEORETICAL ASPECTS

In this section we recall the formalism that will be used in the three-flavor analysis, under the hypothesis that the neutrino mass spectrum is as in Fig. 1. We introduce new graphical representations of the parameter space, and use them to discuss the properties of the three-flavor MSW probability $P(\nu_e \rightarrow \nu_e)$.

A. A simple three-flavor framework and its parameter space

In the general three-generation case, the flavor eigenstates ν_α ($\alpha = e, \mu, \tau$) are a superposition of three mass eigenstates ν_i ($i = 1, 2, 3$): $\nu_\alpha = U_{\alpha i} \nu_i$. The (unitary) neutrino mixing matrix $U_{\alpha i}$ is usually parametrized in the same way as the standard Cabibbo-Kobayashi-Maskawa (CKM) mixing matrix in the quark sector [39], involving three mixing angles, $(\theta_{12}, \theta_{23}, \theta_{13}) \in [0, \pi/2]$, and one CP-violating phase, δ. Redefining the angles as $\omega \equiv \theta_{12}$, $\psi \equiv \theta_{23}$, and $\phi \equiv \theta_{13}$, the standard parametrization reads

$$
\begin{pmatrix} \nu_e \\ \nu_\mu \\ \nu_\tau \end{pmatrix} = \begin{pmatrix} \cos\omega\cos\phi & \sin\omega\cos\phi & \sin\phi e^{-i\delta} \\ -\sin\omega\cos\psi - \cos\omega\sin\psi\sin\phi e^{i\delta} & \cos\omega\cos\psi - \sin\omega\sin\psi\sin\phi e^{i\delta} & \sin\psi\cos\phi \\ \sin\omega\sin\psi - \cos\omega\cos\psi\sin\phi e^{i\delta} & -\cos\omega\sin\psi - \sin\omega\cos\psi\sin\phi e^{i\delta} & \cos\psi\cos\phi \end{pmatrix} \begin{pmatrix} \nu_1 \\ \nu_2 \\ \nu_3 \end{pmatrix}. \tag{2}
$$

Permutations of the mass eigenstate labels (1, 2, 3) do not change the physics, provided that the mixing angles (ω, ψ, ϕ) are left to range in the first quadrant [39]. The parameter set is completed by two independent neutrino square mass differences, that we write as

$$
\delta m^2 \equiv m_2^2 - m_1^2, \quad m^2 \equiv m_3^2 - m_2^2, \tag{3}
$$

so that the general three-flavor parameter space is $(\delta m^2, m^2, \omega, \psi, \phi, \delta)$.

In principle, a complete phenomenological analysis of three-flavor neutrino oscillations should span the entire six-dimensional manifold $(\delta m^2, m^2, \omega, \psi, \phi, \delta)$. This task would be exceedingly difficult—and perhaps not really useful—at this time, due to vastness of the parameter space, as opposed to the scarcity of evidences in favor of neutrino oscillations.

A much more manageable framework is obtained under the simple hypothesis that the mass spectrum has the property shown in Fig. 1: $\delta m^2 \ll m^2$. Figures 1(a) and 1(b) lead to the same solar neutrino physics. We will always refer to Fig. 1(a) in the following, and conventionally label the mass eigenstates in the order of increasing mass ($m_1 < m_2 < m_3$). In this case, as far as solar neutrinos are concerned, the two quasi-degenerate mass eigenstates ν_1 and ν_2 participate actively to matter-enhanced transitions, while the ''lone'' state ν_3 is a spectator neutrino that reveals its presence only through the mixing [40–42].

At zeroth order in $\delta m^2/m^2$, the following properties hold (see [10,13] and references therein): (1) solar neutrino experiments probe only the subspace $(\delta m^2, \omega, \phi)$; (2) terrestrial (i.e., accelerator, reactor, atmospheric) neutrino experiments probe only the subspace (m^2, ψ, ϕ); (3) effects related to the CP-violating phase δ are unobservable, so that the mixing matrix in Eq. (2) can be taken as real for our purposes.

In other words, solar neutrino experiments explore the space $(\delta m^2, U_{e1}^2, U_{e2}^2, U_{e3}^2)$ that is the small mass square difference and the three matrix elements related to ν_e (the fast m^2-driven oscillations being effectively averaged out) [10]. Terrestrial (accelerator, reactor, atmospheric) neutrino experiments explore instead the space $(m^2, U_{e3}^2, U_{\mu3}^2, U_{\tau3}^2)$ that is the large mass square difference and the three matrix elements related to ν_3 (the slow δm^2-driven oscillations being effectively frozen) [13].

The five mixing matrix elements U_{ei} and $U_{\alpha3}$ probed by solar and terrestrial oscillation searches satisfy the two unitarity conditions:

$$
U_{e3}^2 + U_{\mu3}^2 + U_{\tau3}^2 = 1, \tag{4a}
$$

$$
U_{e1}^2 + U_{e2}^2 + U_{e3}^2 = 1. \tag{4b}
$$

In [13] it has been shown that Eq. (4a) can be embedded in a triangular representation of the space spanned by the the ''lone'' neutrino state: $\nu_3 = U_{e3}\nu_e + U_{\mu3}\nu_\mu + U_{\tau3}\nu_\tau$. In Fig. 4, we embed analogously the second unitarity condition, Eq. (4b), in a triangular representation of the space spanned by the electron neutrino state: $\nu_e = U_{e1}\nu_1 + U_{e2}\nu_2 + U_{e3}\nu_3$. The triangle in Fig. 4 has equal sides, unit height, and corners corresponding to the mass eigenstates ν_1, ν_2, ν_3. A generic
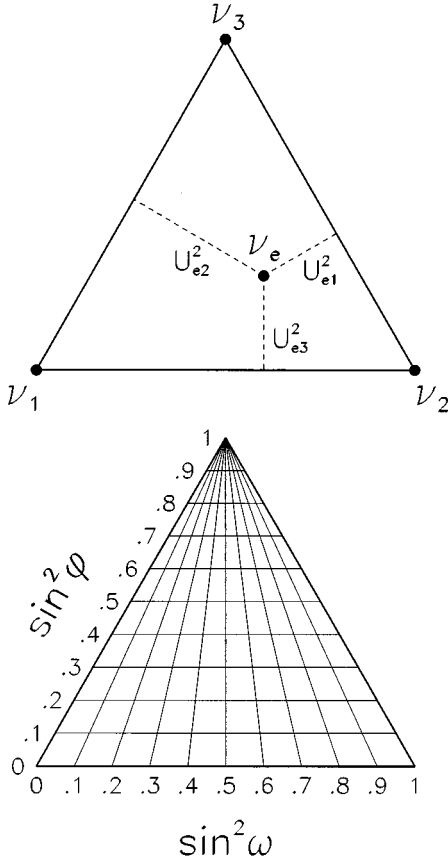
FIG. 4. Triangular plot representing the neutrino state ν_e in terms of its massive components ν_1, ν_2, ν_3. For a triangle of unit height, the unitarity relation $U_{e1}^2 + U_{e2}^2 + U_{e3}^3 = 1$ is enforced by identifying the U_{ei}^2 with the three distances of ν_e from the sides (dashed lines). The usual two-generation oscillation limit is reached for ν_e onto the lower side joining ν_1 to ν_2. Isolines of $\sin^2\omega$ and $\sin^2\phi$ (parametrizing the elements U_{ei}^2) are charted in the lower plot.
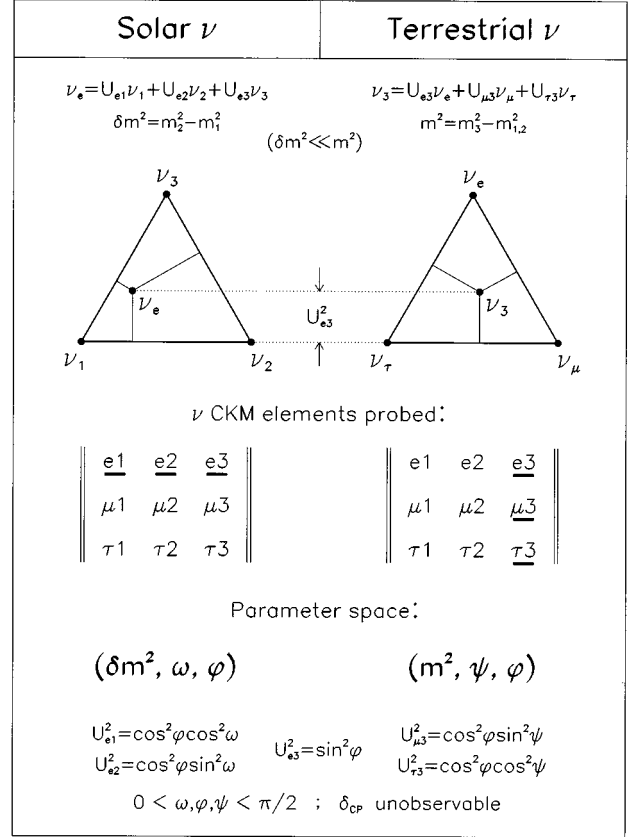

FIG. 5. A synoptic presentation of the parameter space for solar and terrestrial (accelerator, reactor, atmospheric) neutrino oscillation searches. Solar neutrinos probe the small square mass difference, δm^2, and the mixing matrix elements U_{ei}^2. Terrestrial neutrinos probe the large square mass difference, m^2, and the mixing matrix elements $U_{\alpha 3}^2$. Notice that U_{e3}^2 is probed in both cases, whilst the CP-violating phase δ is unobservable. The expansion of $U_{\alpha i}^2$ in terms of the mixing angles (ω, ϕ, ψ) is shown. The reader is referred to the text and to [13] for further details.

state ν_e is represented by a point in the triangle. The U_{ei}^2 are identified with the heights projected from ν_e. The sum of such heights is always equal to the total (unit) height of the triangle. In Fig. 4 we also chart, in the lower subplot, the triangle coordinates in terms of ω and ϕ. The usual two-generation limit is reached for $\phi = 0$, that is for ν_e on the side joining ν_1 to ν_2 (and thus decoupled from ν_3).

In Fig. 5 we show a synoptic presentation of the two triangular graphs introduced in Fig. 4 of this work and in Fig. 2 of [13]. On the left (right) side we display the parametrization of solar (terrestrial) neutrino oscillations, including the expansion of the relevant mixing matrix elements in terms of the mixing angles. Note that both solar and terrestrial neutrinos probe the element U_{e3}, i.e., the angle ϕ, as discussed in [10–13] and also in [43,44]. This important link between the experiments sensitive to δm^2 (solar) and those sensitive to m^2 (terrestrial) will be utilized in Sec. IV.

B. Electron neutrino survival probability

The electron neutrino survival probability, $P(\nu_e \rightarrow \nu_e)$, is the fundamental quantity to compute in the solar neutrino analysis. In this section we study some properties of the

three-flavor MSW survival probability, $P_{3\nu}^{\text{MSW}}$ as a function of ω, ϕ, and $\delta m^2/E_\nu$ (E_ν being the neutrino energy). We start with a brief review of a well-known analytical approximation to $P_{3\nu}^{\text{MSW}}$ that has been used in the present work. In order to avoid unnecessary complications, in this section and in the related figures we ignore temporarily the smearing of $P_{3\nu}^{\text{MSW}}$ over the neutrino production region, and the earth regeneration effect. These effects will be included, however, in the global analysis of Sec. IV.

In the limit $\delta m^2 \ll m^2$, the probability $P_{3\nu}^{\text{MSW}}$ takes the simple form [40,5]

$$P_{3\nu}^{\text{MSW}} = \cos^4\phi P_{2\nu}^{\text{MSW}} + \sin^4\phi, \qquad (5)$$

where $P_{2\nu}^{\text{MSW}}$ is the MSW probability in the two-generation limit, provided that the solar electron density $N_e(x)$ at any point x is effectively replaced by $N_e(x)\cos^2\phi$.

A very accurate and widely used analytical approximation to $P_{2\nu}^{\text{MSW}}$ is the so-called ''Parke's formula'' [45]:

$$P_{2\nu}^{\text{MSW}} = \frac{1}{2} + \left(\frac{1}{2} - \Theta P_C\right)\cos 2\omega \cos 2\omega_m^0. \qquad (6)$$

This approximation was also studied by other authors [46]. In Eq. (6), P_C is the Landau-Zener-Stueckelberg crossing probability [47], that we use in the improved form [48,49] valid for a close-to-exponential radial density; ω_m^0 is the mixing angle in matter at the production point. The step function Θ [27] switches from 0 (nonresonant propagation case) to 1 (resonant propagation case) if the mixing angle ω in matter can assume the value $\pi/4$ at a point x along the neutrino trajectory in the sun:

$$\omega_m(x) = \frac{\pi}{4} \iff \delta m^2 \frac{\cos 2\omega}{\cos^2 \phi} = 2\sqrt{2} G_F N_e(x) E_\nu. \quad (7)$$

Equation (7) numerically reads

$$\frac{\delta m^2}{\text{eV}^2} \frac{\cos 2\omega}{\cos^2 \phi} = 1.60 \times 10^{-5} \frac{E_\nu}{\text{MeV}} \frac{N_e(x)}{N_e(0)}, \quad (8)$$

where $N_e(0)$ is the electron density at the center of the sun [19].

A technical remark is in order. In the literature, the numerical validity of the approximations implicit in Eq. (6) has been discussed [49,50] mainly for ω (and ϕ [27]) in the first octant $[0, \pi/4]$. Since we are interested in analyzing the full mixing angle space (the first quadrant), we have calculated the function $P_{3\nu}^{\text{MSW}} = P_{3\nu}^{\text{MSW}}(\delta m^2/E_\nu)$ with a Runge-Kutta integration of the three-flavor MSW equations, for a number of representative (ω, ϕ) values in $[0, \pi/2]$. The agreement between the analytical approximation of Eqs. (5) and (6) and the ''exact'' (but much more time-consuming) Runge-Kutta calculation is as good in the second octant as it is in the first, provided that $\delta m^2/E_\nu$ is taken above $\sim 10^{-8}$ eV^2/MeV. For values of $\delta m^2/E_\nu$ lower than $\sim 10^{-8}$ eV^2/MeV, one should more properly consider just-so vacuum oscillations [51].

There are a few interesting limits for $P_{3\nu}^{\text{MSW}}$. If $\delta m^2/E_\nu \gg 10^{-5}$ eV^2/MeV, the MSW mechanism is not effective and $P_{3\nu}^{\text{MSW}}$ tends to its vacuum value $P_{3\nu}^{\text{vac}}$ given by

$$P_{3\nu}^{\text{vac}} = \cos^4 \phi P_{2\nu}^{\text{vac}} + \sin^4 \phi = \cos^4 \phi \left(1 - \frac{1}{2}\sin^2 2\omega\right) + \sin^4 \phi$$

$$= 1 - 2(U_{e1}^2 U_{e2}^2 + U_{e2}^2 U_{e3}^2 + U_{e3}^2 U_{e1}^2), \quad (9)$$

where the fast $(\delta m^2/E_\nu)$-driven oscillations have been averaged to 1/2.

Given the above expression for $P_{3\nu}^{\text{vac}}$ and Eqs. (5) and (6) for $P_{3\nu}^{\text{MSW}}$, it follows that $P_{3\nu}^{\text{MSW}} = P_{3\nu}^{\text{vac}}$ for arbitrary values of $(\delta m^2/E_\nu)$, in (at least) three cases:

$$\omega = 0 \rightarrow P_{3\nu}^{\text{MSW}} = \cos^4 \phi + \sin^4 \phi = P_{3\nu}^{\text{vac}}, \quad (10a)$$

$$\omega = \frac{\pi}{4} \rightarrow P_{3\nu}^{\text{MSW}} = \frac{1}{2}\cos^4 \phi + \sin^4 \phi = P_{3\nu}^{\text{vac}}, \quad (10b)$$

$$\omega = \frac{\pi}{2} \rightarrow P_{3\nu}^{\text{MSW}} = \cos^4 \phi + \sin^4 \phi = P_{3\nu}^{\text{vac}}. \quad (10c)$$

The above properties are exact, i.e., they do not depend on the approximations implicit in Eq. (6). A subcase of Eq.
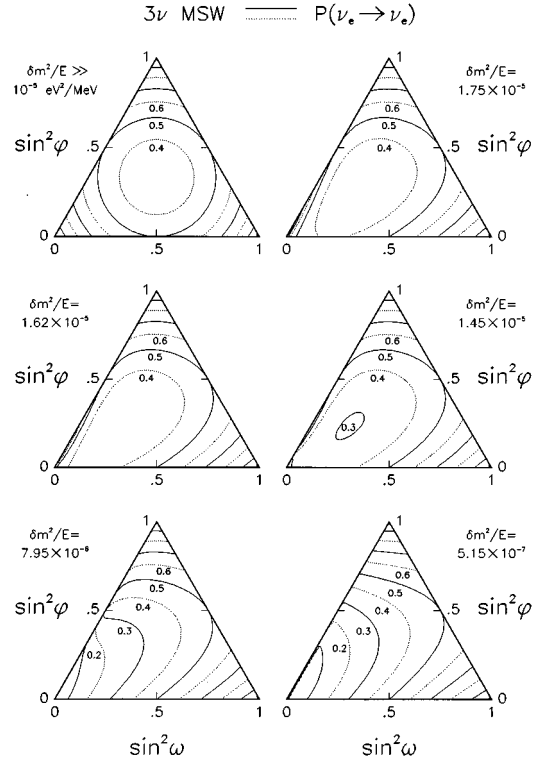

FIG. 6. Isolines of survival probability $P(\nu_e \rightarrow \nu_e)$ in the triangular plot defined in Fig. 4, for six representative values of $\delta m^2/E_\nu$. The first subplot represents the averaged vacuum oscillation case. In the other subplots, the MSW effect is active and produces an increasing deformation of the curves as ν_e approaches ν_3 (the left lower corner). For $\omega = 0, \pi/4, \pi/2$, however, the probability remains equal to the vacuum value, as discussed in the text. (The behavior at $\omega \simeq 0$ cannot be graphically resolved in the last two subplots.)

(10b) is obtained in the ''maximal mixing scenario'' [52], corresponding to the center of the triangle in Fig. 4 ($\sin^2 \omega = 1/2$, $\sin^2 \phi = 1/3$).

A further property follows from Eqs. (5), (6), and (9):

$$P_{3\nu}^{\text{MSW}}\big|_{\omega_m^0 = \pi/4} = \frac{1}{2}\cos^4 \phi + \sin^4 \phi = P_{3\nu}^{\text{vac}}\big|_{\omega = \pi/4}. \quad (11)$$

This property, however, is not exact and has the same limits of validity of Eq. (6) (see also the discussion at the end of this section).

Equations (9)–(11) are helpful in understanding the behavior of $P_{3\nu}^{\text{MSW}}$ as a function of its arguments $(\delta m^2/E_\nu, \omega, \phi)$, as we discuss now in some detail.

In Fig. 6, curves of constant $P_{3\nu}^{\text{MSW}}$ are shown for selected values of $\delta m^2/E_\nu$ in the triangular representation. In the first subplot $(\delta m^2/E_\nu \gg 10^{-5}$ eV^2/MeV), it is $P_{3\nu}^{\text{MSW}} = P_{3\nu}^{\text{vac}}$ in the whole triangle, and the isoprobability curves are circles [as it is easily derived from Eq. (9)], with a minimum value $P_{3\nu} = 1/3$ at the triangle center. In the second subplot $(\delta m^2/E_\nu = 1.75 \times 10^{-5}$ eV^2/MeV), the curves begin to be deformed by the MSW effect for ν_e close to ν_1 (the low left corner). Notice, however, that just along the lines at $\omega = 0, \pi/4, \pi/2$ (refer to Fig. 4 also) the probability takes the same values as in the previous plot ($P_{3\nu}^{\text{MSW}} = P_{3\nu}^{\text{vac}}$), as ex-
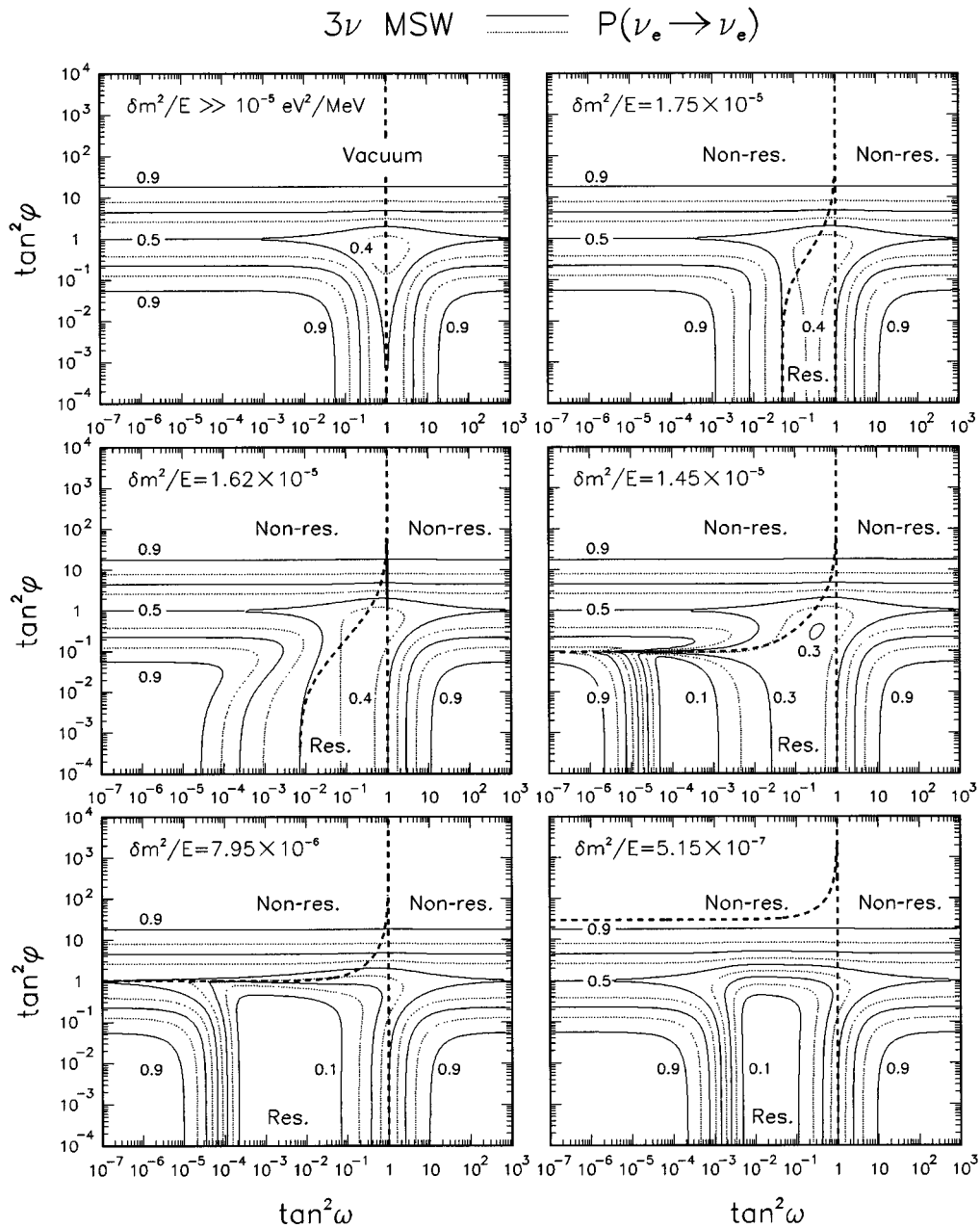
FIG. 7. As in Fig. 6, but in the bilogarithmic $(\tan^2\omega, \tan^2\phi)$ representation. Notice the deformation of the isoprobability contours due to the $\triangle \to \square$ mapping. In this representation the ν_1, ν_2, ν_3 mass eigenstates are reached respectively in the limits: $\tan^2\phi \to 0$ and $\tan^2\omega \to 0$; $\tan^2\phi \to 0$ and $\tan^2\omega \to \infty$; $\tan^2\phi \to \infty$ at any $\tan^2\omega$. The thick, dashed lines represents the curves for maximal ω-mixing in vacuum and matter: $\omega = \pi/4$ (vertical) and $\omega_m^0 = \pi/4$ (curve on the left). These two curves separate the zones where the neutrino propagation is nonresonant from those where it is resonant.

pected from Eqs. (10a)–(10c). These properties also hold for the remaining four subplots where, however, the increasingly important MSW effect prevents a graphical resolution of the isolines at small ω values, i.e., close to the left side of the triangle.

In Fig. 7 we map the triangular parameter space onto a ''square'' bilogarithmic plot with coordinates $(\tan^2\omega, \tan^2\phi)$. This new representation has the advantage that the ''triangle corners'' are infinitely expanded, although the nice symmetry properties of the triangular representation are lost. A similar representation was introduced in [13] to map the parameter space of terrestrial neutrinos. The values of $\delta m^2/E_\nu$ and the isoprobability curves in Fig. 7 correspond

exactly to those in Fig. 6. In Fig. 7 we also draw two curves (thick, dashed lines) corresponding to $\omega_m^0 = \pi/4$ [Eq. (7) with $x=0$] and $\omega = \pi/4$. These curves separate the zones where the propagation is nonresonant from those where it is resonant, as indicated in all panels. The behavior of $P_{3\nu}^{\mathrm{MSW}}$ is most interesting near the curve at $\omega_m^0 = \pi/4$ and in the resonance region. Notice, for the subplots at $\delta m^2/E_\nu = 1.45 \times 10^{-5}$ eV^2/MeV or lower, the appearance of a depletion zone for $P_{3\nu}^{\mathrm{MSW}}$ at small values of ω (the ''small angle MSW solution'').

In Fig. 7, the properties expressed by Eqs. (10a) and (10b) can be easily checked. The implications of Eq. (11) are instead more subtle; if one takes any two points at the same
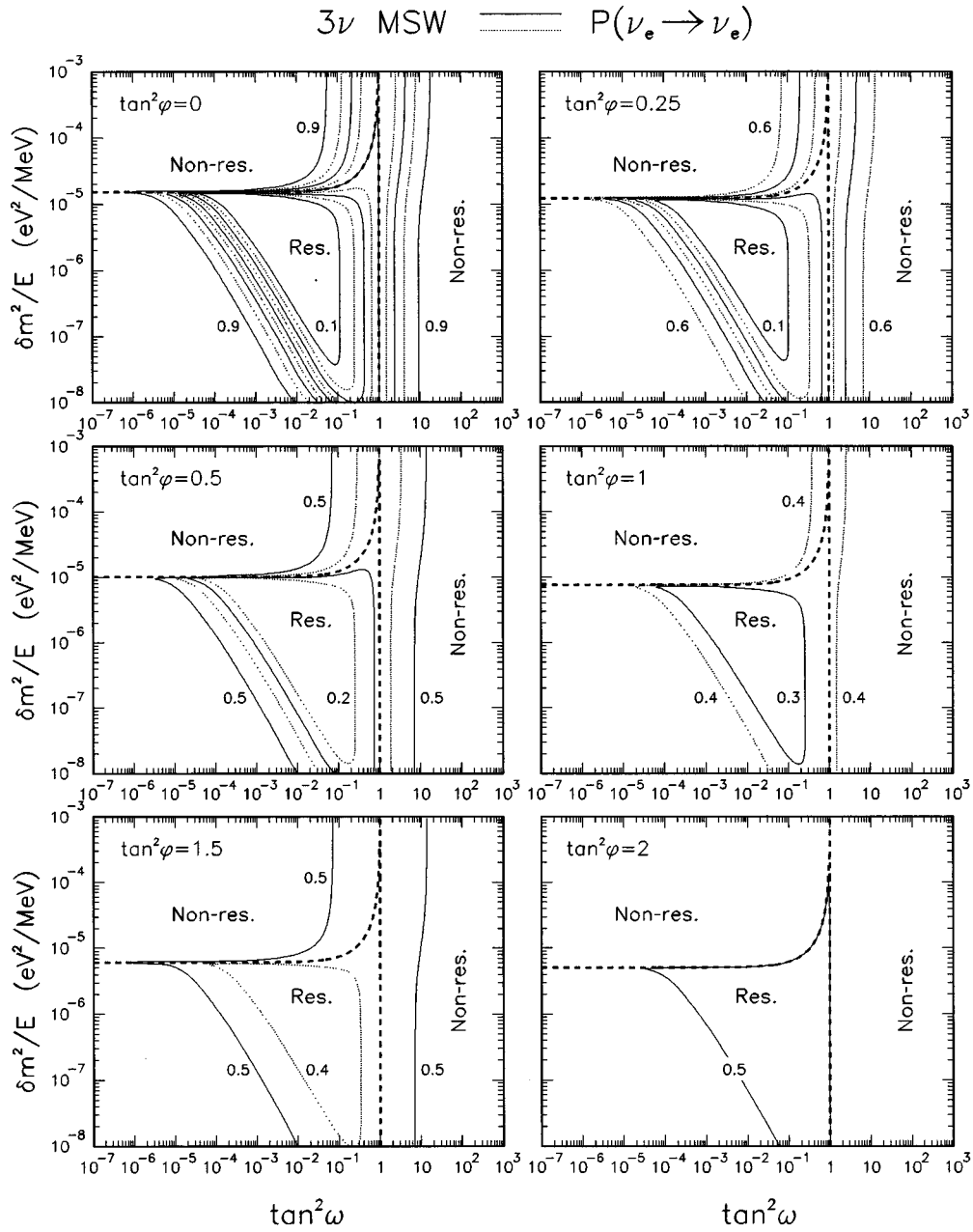
FIG. 8. Isolines of survival probability $P(\nu_e \rightarrow \nu_e)$ in the bilogarithmic $(\tan^2\omega, \delta m^2/E_\nu)$ plane, for representative values of $\tan^2\phi$. The thick, dashed curves are defined as in Fig. 7. The resonant region has the characteristic triangular shape. The variations of $P(\nu_e \rightarrow \nu_e)$ in the plane decrease for increasing ϕ.

height (same ϕ) on the dashed curves ($\omega = \pi/4$ and $\omega_m^0 = \pi/4$), then the probabilities $P_{3\nu}$ at these conjugate points are equal. It may be said, in a figurative way, that the MSW mechanism "cuts" the (ω, ϕ) plane along the dashed lines at $\omega = \pi/4$ and $\omega_m^0 = \pi/4$, "separates" the edges (that would coincide for vacuum oscillations) and "fills" the cut zone with a new resonant region where the survival probability can be much lower than in the vacuum case. The probabilities in the "old" regions at the right and left of the two dashed lines are only weakly (adiabatically) different from the corresponding vacuum oscillation values.

We finally show in Fig. 8 the behavior of $P_{3\nu}^{\text{MSW}}$ for six representative values of ϕ, in a bilogarithmic $(\delta m^2/E_\nu, \tan^2\omega)$ mass-mixing plane (a perhaps more famil-

iar representation). As in the previous figure, the two thick, dashed lines correspond to the curves at $\omega = \pi/4$ and $\omega_m^0 = \pi/4$, that separate nonresonant and resonant propagation regions. The curves of isoprobability in the resonant region have the characteristic triangular shape [26]. Notice that the variations of $P_{3\nu}^{\text{MSW}}$ within the mass-mixing plane decrease as ϕ increases and the MSW effect is suppressed.

A final remark about the calculation of the survival probability. As shown in [49], Eq. (6) is a good approximation except for the particular case of a neutrino created close to the resonance ($\omega_m^0 \simeq \pi/4$) *and* with very small vacuum mixing ($\tan^2\omega \lesssim 10^{-4}$). This situation would correspond to a very narrow strip, localized along the thick, dashed curves in Figs. 7 and 8 for $\tan^2\omega \lesssim 10^{-4}$. The local discrepancy with
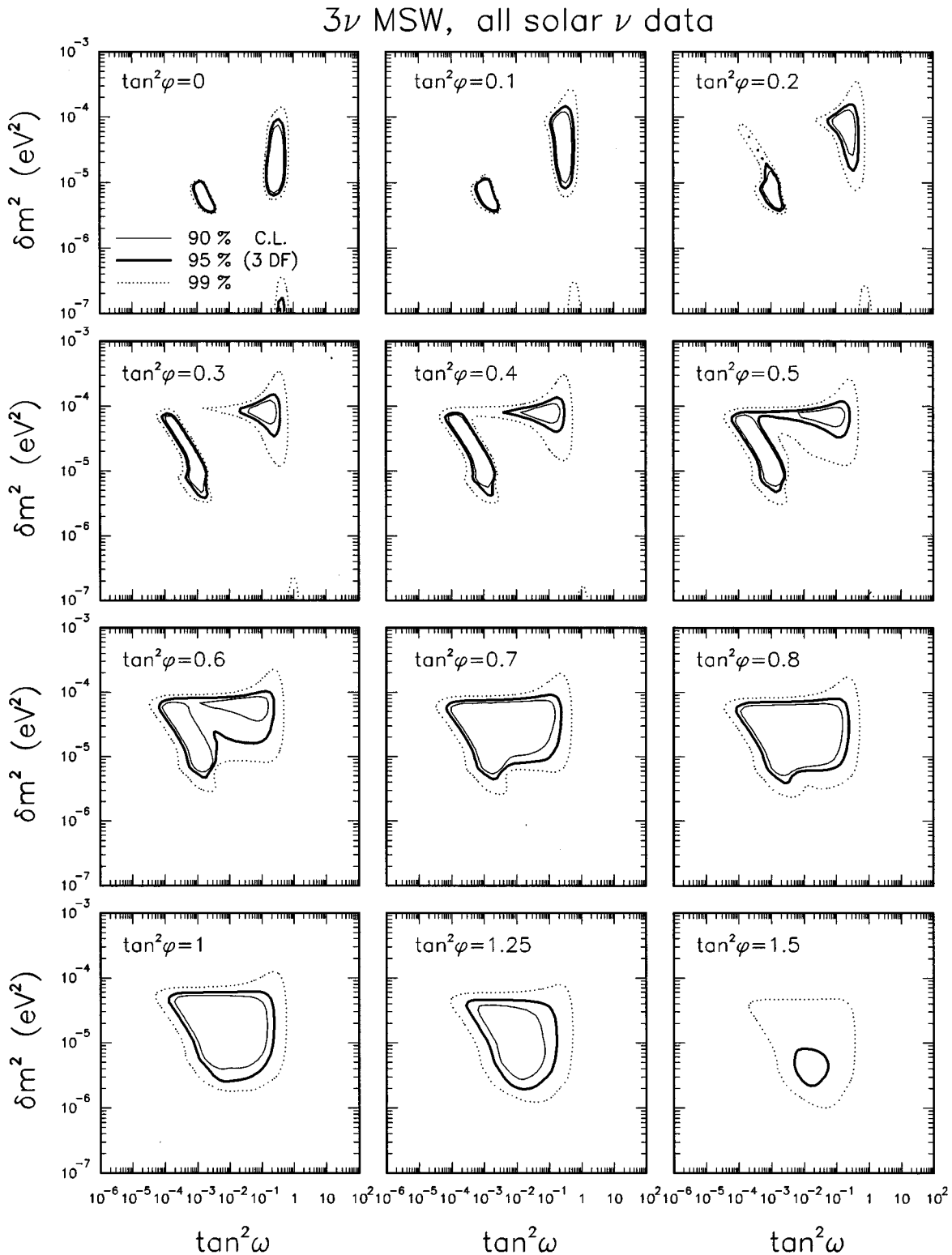
FIG. 9. Three-flavor MSW analysis of all solar neutrino data. The regions allowed at 90%, 95%, 99% C.L. in the space $(\delta m^2, \tan^2\omega, \tan^2\phi)$ are shown in planar $(\delta m^2, \tan^2\omega)$ sections at twelve representative values of $\tan^2\phi$ ranging from 0 to 1.5. The two-generation limit is recovered at $\tan^2\phi = 0$ (first subplot). The two separate solutions at small ϕ merge in one single solution for increasing ϕ. See the text for details.

the exact probability is, however, unimportant in the calculation of the neutrino rates, being effectively suppressed by the integration over the neutrino production region and energy spectrum, and being confined to values of ω where no solution to the solar neutrino problem is found.

IV. THREE-FLAVOR MSW SOLAR NEUTRINO OSCILLATIONS: PHENOMENOLOGY

In this section we present the results of our global three-flavor MSW analysis of solar neutrino data (Table I) in the

parameter space $(\delta m^2, \omega, \phi)$. We span the coordinates $\delta m^2 \otimes \tan^2 \omega \otimes \tan^2 \phi$ in the range $[10^{-7}\text{eV}^2, 10^{-3}\text{eV}^2]$ $\otimes [10^{-6}, 10^{-2}] \otimes [10^{-4}, 10^4]$ and analyze the data through a χ^2 statistic, including experimental and theoretical errors and their correlations.

We find the absolute minimum, $\chi^2_{\min} = 0.74$, at $\delta m^2 = 5.21 \times 10^{-6}$ eV^2, $\omega = 2.57°$, $\phi = 0°$. It coincides with the minimum of the two-generation analysis (Sec. II B). The surfaces at $\chi^2 = \chi^2_{\min} + \Delta\chi^2$, with $\Delta\chi^2 = 6.25$, 7.82, and 11.34, define the regions allowed at 90%, 95%, and 99% C.L. for three degrees of freedom. We present representative sections of these three-dimensional allowed regions in the bilogarithmic mass-mixing plane $(\delta m^2, \tan^2\omega)$ at several values of $\tan^2\phi$, and in the bilogarithmic mixing-mixing plane $(\tan^2\omega, \tan^2\phi)$ at several values of δm^2. We also show representative fits to separate pieces of data. We finally discuss how this solar neutrino analysis is linked to the terrestrial neutrino oscillation constraints obtained in [13].

A. Analysis in the mass-mixing plane

In Fig. 9 we show the sections of the allowed regions in the bilogarithmic plane $(\tan^2\omega, \delta m^2)$, for representative values of $\tan^2\phi$. Notice than both ω and ϕ are allowed to range above the first octant in the fit. In the first panel, $\tan^2\phi$ is zero and purely two-generation oscillations take place. In fact, this subplot is a mapping of Fig. 3, modulo the different number of degrees of freedom in the definition of the C.L. contours. A moderate increase of $\tan^2\phi$ from 0.1 up to 0.4 produces an increasing deformation of the allowed contours. The contours tend to merge in the upper part, corresponding to the upper side of the MSW "triangles" of Fig. 8. The two separate solutions merge in a single connected solution at $\tan^2\phi \simeq 0.5$, as also shown in [7,9]. For increasing value of $\tan^2\phi$, the allowed region becomes broader and less structured, and then rapidly shrinks and disappears at $\tan^2\phi \gtrsim 1.5$. Figure 8 helps in understanding the flattening of the allowed region in Fig. 9 at the higher values of $\tan^2\phi$.

From Fig. 9 it can be noticed that, although there are no solutions for $\omega > \pi/4$, the fit can still be acceptable for $\phi > \pi/4$. In Fig. 10 we then show the values of $\chi^2 - \chi^2_{\min}$ as a function of $\tan^2\phi$, for δm^2 and $\tan^2\omega$ unconstrained. The minimum is reached at $\phi = 0°$, meaning that the two-generation limit is preferred by the present data. However, three-flavor solutions are allowed for values of $\tan^2\phi$ as high as 1.4 (i.e., $\phi \simeq 50°$) at 90% C.L. There are no acceptable solutions at 99% C.L. for $\tan^2\phi \gtrsim 2$.

The behavior of the solutions in Fig. 9 can be understood better by separating the information coming from single pieces of data. In Fig. 11 we show the separate fits to the gallium, chlorine, and Kamiokande (total rate and night-day asymmetry) measurements, in the same coordinates as in Fig. 9, for three values of $\tan^2\phi$. The thick, solid line represents contours at 95% C.L. The allowed regions are marked by stars. The dotted lines represent contours of isosignal. The structured shape of the isosignal curves is globally similar to the isoprobability curves in Fig. 8. The regions allowed by the separate pieces of data become wider for increasing ϕ, and even extend above $\omega = \pi/4$, but their mutual compatibility do not necessarily increase. In particular, notice in Fig. 11 that the chlorine data play a major role in confining ω below
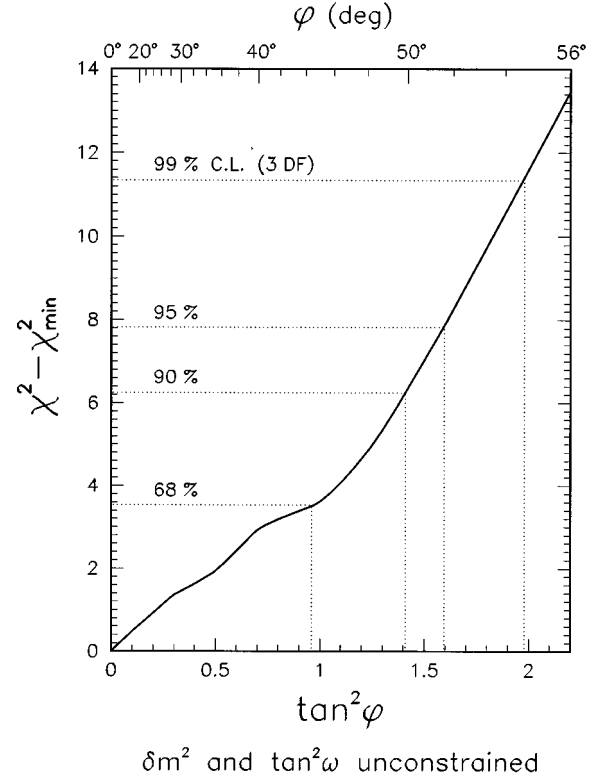

FIG. 10. Values of $\Delta\chi^2$ as a function of $\tan^2\phi$, for δm^2 and $\tan^2\omega$ unconstrained. The value $\phi = 0$, corresponding to the two-generation limit, is preferred, but values as high as $\tan^2\phi \simeq 1.4$ ($\phi \simeq 50°$) are still allowed at 90% C.L.

$\pi/4$ in the global fit of Fig. 9.

We have found three-flavor solutions to the solar neutrino problem at relatively large ϕ. These solutions are characterized by a survival probability, $P_{3\nu}^{\text{MSW}}$ that varies more slowly with energy as compared to the two-generation case (see Fig. 8). Probing the large-ϕ three-flavor solutions will therefore represent a formidable challenge to the new generation of solar neutrino experiments, SuperKamiokande [53], the Sudbury Neutrino Observatory (SNO) [54], and the Imaging of Cosmic and Rare Underground Signals (ICARUS) [55], that are meant to probe the energy dependence of the solar neutrino flux at earth.

B. Analysis in the mixing-mixing plane

In Fig. 12 we show the sections of the allowed region in the mixing-mixing plane $(\tan^2\omega, \tan^2\phi)$ for representative values of δm^2. In all panels, the two-generation limit is reached for $\tan^2\phi \to 0$ (lower side), and the solutions lie along one or more of a three-sided ⊓-shaped band. The sides correspond to "small ω," "large ω," and "large ϕ" solutions. The "small ω" and "large ω" solutions protrude in the three-flavor space from the usual MSW solutions in the two-generation limit. The "large ϕ" solution is genuinely three-flavor and corresponds to the horizontal depletion zone of the survival probability $P_{3\nu}^{\text{MSW}}$ in Fig. 7. In the first two and last two subplots there is no solution in the two-generation limit.

In Fig. 13 we show the fits to single experimental data, in the same coordinates as in Fig. 12, for three values of δm^2.
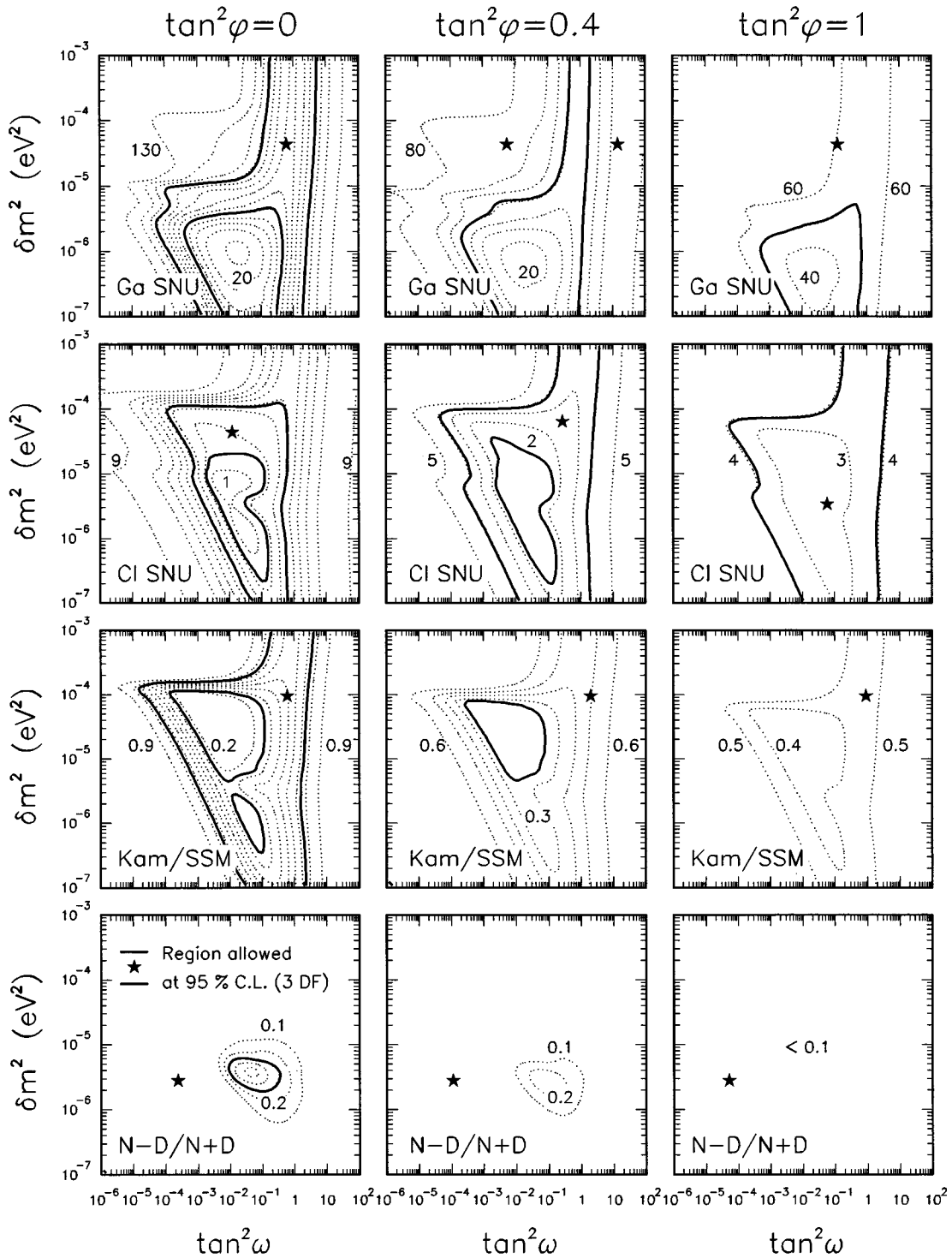
FIG. 11. Three-flavor MSW analysis of individual neutrino data in the same coordinates as in Fig. 9, for three representative values of $\tan^2\phi$. The solid lines correspond to 95% C.L. contours. The allowed regions are marked by stars. Dotted lines represent iso-signal contours.

As in Fig. 11, the thick, solid lines correspond to iso-$\Delta\chi^2$ contours at 95% C.L., and the dotted lines represent isosignal curves. The allowed regions are marked by stars. Notice how, in all cases, the solutions in the two-generation limit (lower side, $\phi\to 0$) merge as ϕ increases.

C. Solar neutrinos vs accelerator and reactor neutrinos

In this work we have found and discussed the MSW solutions to the solar neutrino problem in the parameter space $(\delta m^2, \tan^2\omega, \tan^2\phi)$. In the work [13], the results of the established accelerator and reactor neutrino oscillation searches
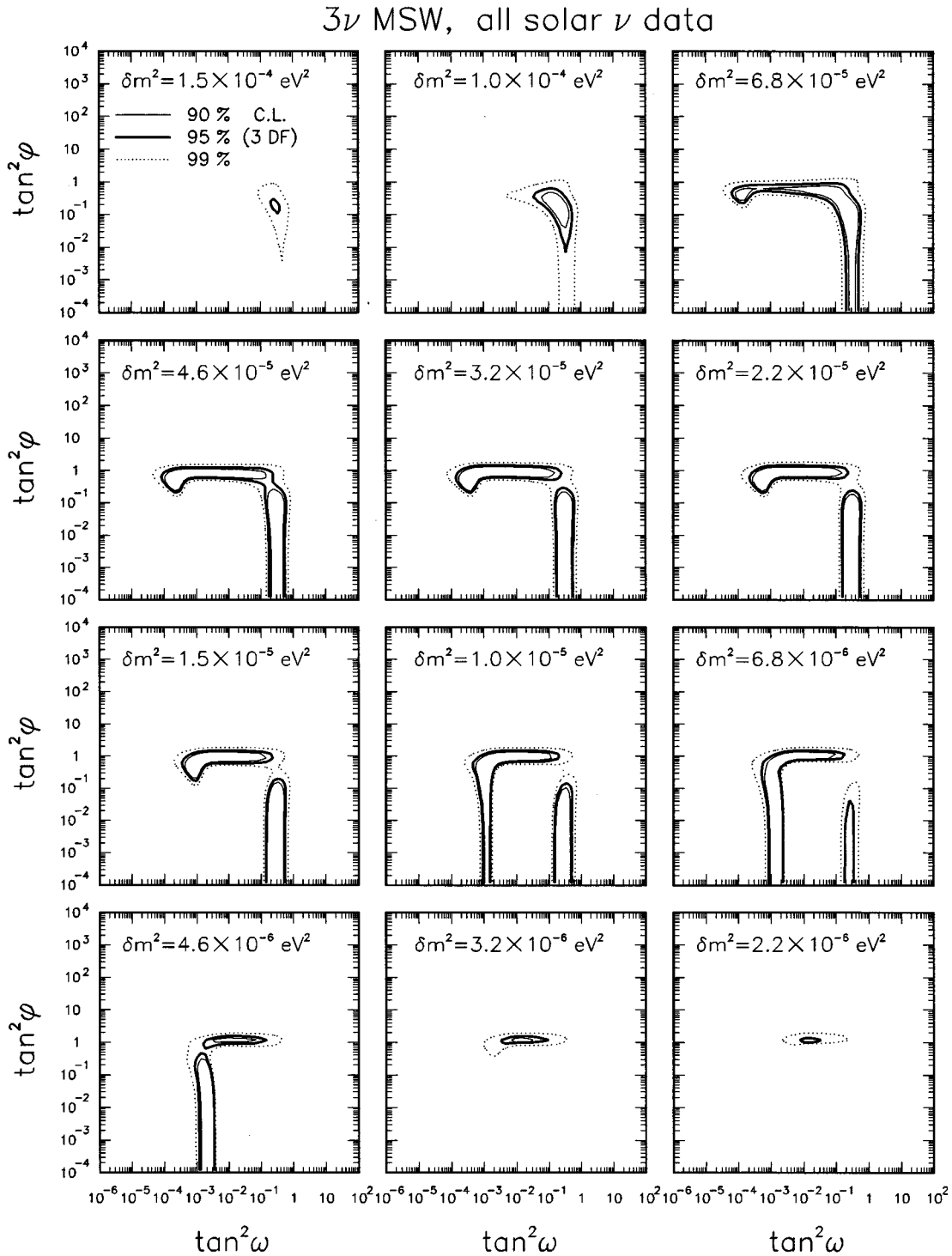
3ν MSW, all solar ν data

FIG. 12. Results of the three-flavor MSW analysis of all solar neutrino data. The regions allowed at 90%, 95%, 99% C.L. in the space $(\delta m^2, \tan^2\omega, \tan^2\phi)$ are shown in planar $(\tan^2\omega, \tan^2\phi)$ sections at twelve representative values of δm^2 ranging from 1.5×10^{-4} to 2.2×10^{-6} eV^2. The two-generation limit is recovered for $\tan^2\phi \rightarrow 0$ (lower side of each subplot). Notice the appearance of solutions disconnected from the two-generation limit. See the text for details.

were analyzed in order to constrain the parameter space $(m^2, \tan^2\psi, \tan^2\phi)$. Both works are based on one, and only one, hypothesis about the neutrino spectrum, namely $\delta m^2 \ll m^2$ (as in Fig. 1). The angle ϕ is common to both spaces $(\delta m^2, \tan^2\omega, \tan^2\phi)$ and $(m^2, \tan^2\psi, \tan^2\phi)$, as also evidenced in Fig. 5.

We invite the reader to place, side-by-side, Fig. 12 of this work and Fig. 10 of [13], in the way suggested by Fig. 5.

These two figures provide us with 12×12 combinations of $(\delta m^2, m^2)$. For any given couple of square mass differences $(\delta m^2, m^2)$, one can find in these two figures the allowed regions in the $(\tan^2\omega, \tan^2\phi)$ and $(\tan^2\psi, \tan^2\phi)$ mixing-mixing planes. We have purposely chosen the same vertical scale (same decades in $\log\tan^2\phi$) in both cases. The obvious condition that $\tan^2\phi$ (the vertical coordinate) must be the same in both figures imposes a strong compatibility con-
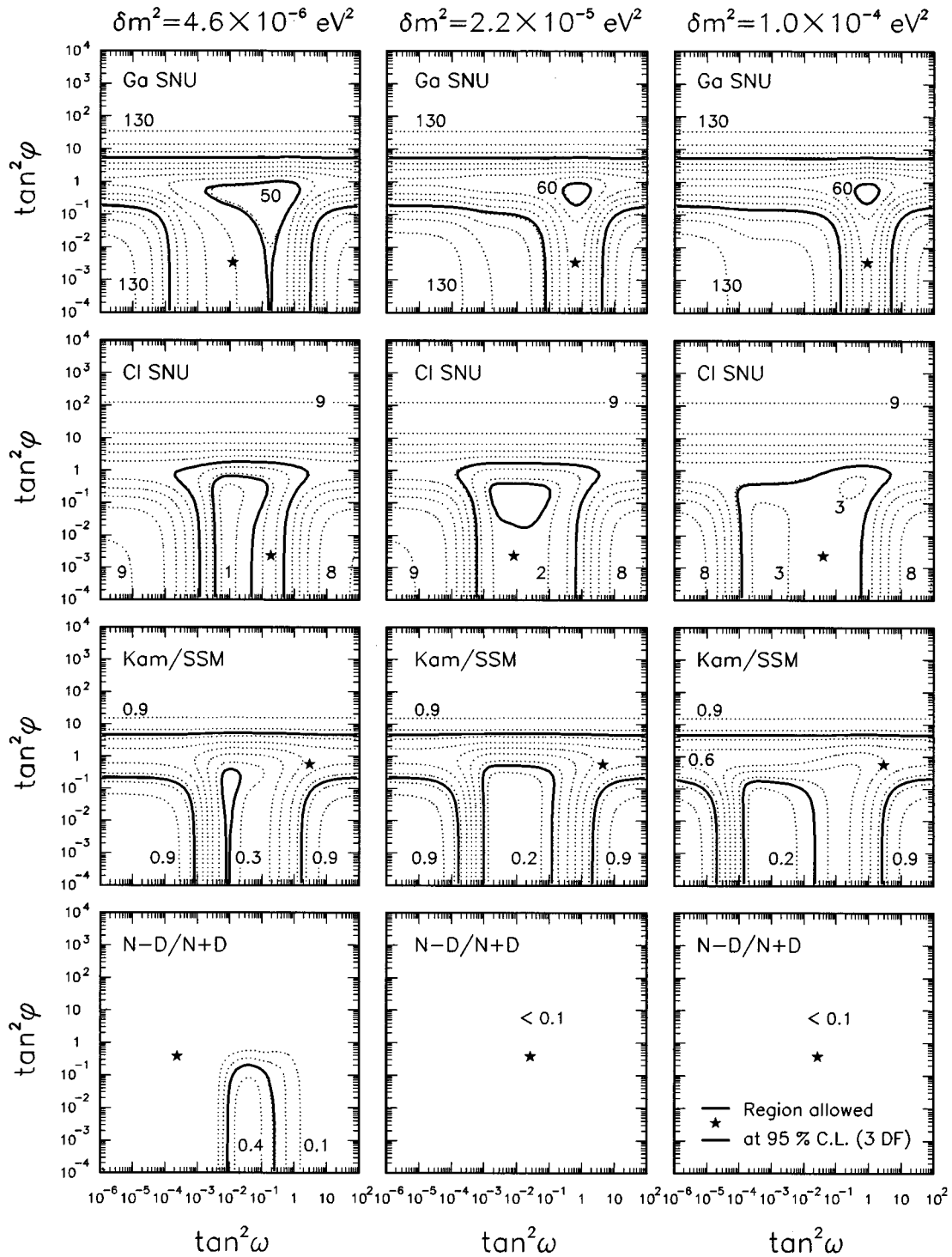
FIG. 13. Results of the three-flavor MSW analysis of individual neutrino data in the same coordinates as in Fig. 12 for three representative values of δm^2. The solid lines correspond to 95% C.L. contours. The allowed regions are marked by stars. Dotted lines represent iso-signal contours.

straint. This constraint eliminates some of the solutions that are individually allowed by solar or terrestrial neutrino oscillation searches. For instance, the regions allowed by accelerator and reactor data at very large $\tan^2\phi$ (i.e., $\phi \to \pi/2$) are never allowed by solar neutrino data, that keep $\tan^2\phi$ below

~ 1.5. In other words, if m^2 is in the range of sensitivity of accelerator and reactor oscillation searches, then the comparison of terrestrial and solar data requires relatively small values of ϕ. Another example is that the MSW-allowed values $\delta m^2 \simeq 1.5 \times 10^{-4}$ eV^2 and $\delta m^2 \simeq (2.2$–$3.2) \times 10^{-6}$ eV^2

are not compatible with accelerator and reactor data for $m^2 \gtrsim 10^{-2}$ eV^2. One can explore various other (in)compatibility situations for the 12×12 cases of $(\delta m^2, m^2)$ that can be extracted from the figures discussed above.

We recall that the only hypothesis adopted in our analysis is $\delta m^2 \ll m^2$. Virtually, all seesaw models of neutrino mass generation satisfy this condition. Model builders can thus check if their favorite values of $(\delta m^2, m^2, \omega, \psi, \phi)$ fall in the allowed regions determined in this work and in [13]. Here we discuss briefly the ''threefold maximal mixing'' model, recently investigated in [56].

The maximal mixing scenario is realized in the centers of the triangles in Fig. 5, that is for $U_{ei}^2 = U_{\alpha 3}^2 = 1/3$ or, equivalently, for $(\tan^2 \omega, \tan^2 \psi, \tan^2 \phi) = (1, 1, 1/2)$. Figure 9 shows that the combination $(\tan^2 \omega, \tan^2 \phi) = (1, 1/2)$ is excluded at more than 99% C.L. by solar ν data (within the MSW approach). The maximal mixing scenario could be reconciled with solar ν data only by dropping the Homestake measurement, that keeps ω below $\pi/4$. From Fig. 10 in [13], it follows that accelerator and reactor data exclude the maximal mixing combination $(\tan^2 \psi, \tan^2 \phi) = (1, 1/2)$ for all values of m^2 in their present sensitivity range ($m^2 \gtrsim 10^{-2}$ eV^2). Thus, the maximal mixing is not supported by all solar neutrino data, and is (trivially) compatible with accelerator and reactor experiments only below their present m^2-sensitivity limits.

V. SUMMARY AND CONCLUSIONS

We have discussed the three-flavor MSW mechanism, in the hypothesis $\delta m^2 \ll m^2$ and for mixing angles ω and ϕ in their maximal range $[0, \pi/2]$. New useful graphical representations of the parameter space (Figs. 4–6) have been introduced. A complete analysis of present data in the mass-mixing space $(\delta m^2, \omega, \phi)$ has been performed, and the solutions have been thoroughly discussed. The data favor the two-generation limit ($\phi = 0°$), but a wide range of three-flavor solutions are allowed up to $\phi \simeq 50°$. The main results are summarized in Figs. 9 and 12.

The ν_e oscillation probability has been studied as a function of the mass and mixing parameters (Figs. 7 and 8). In the allowed regions at large ϕ, the three-flavor probability varies more slowly with energy than in the two-generation case. Thus, it will be difficult to study the large-ϕ solutions in the future solar neutrino experiments that are meant to probe the energy dependence of the solar neutrino flux.

It has been shown that the solar neutrino results are linked to those obtained in an analysis of accelerator and reactor neutrino oscillation searches [13], where the mass-mixing space (m^2, ψ, ϕ) has been thoroughly explored (Fig. 5). This link can be used to further constrain the allowed ranges of the parameters. In particular, for $m^2 \gtrsim 10^{-2}$ eV^2, the angle ϕ is constrained to relatively small values. The threefold maximal mixing scenario [56] is disfavored by solar neutrino data (in the whole explored range of δm^2) as well as by accelerator and reactor experiments for $m^2 \gtrsim 10^{-2}$.

The present study and the work in [13] represent a detailed and accurate analysis of solar, accelerator, and reactor neutrino oscillations in three-flavors. The analysis has made it possible to obtain significant bounds in the mass-mixing parameter space $(\delta m^2, m^2, \omega, \psi, \phi)$.

When this work was completed, we become aware of a recent three-flavor analysis of solar neutrino data performed by Narayan *et al.* in [57]. We agree only qualitatively on their results about the MSW solutions. We do not agree on the precise shape of the allowed regions, and do not confirm their claim that the solutions are dramatically enlarged when the confidence level is moderately increased (from 1σ to 1.6σ in their work). The information contained in [57] is not detailed enough to trace the differences.

[1] LEP Collaborations, ALEPH, DELPHI, L3, and OPAL, Phys. Lett. B **276**, 247 (1992).

[2] M. Gell-Mann, P. Ramond, and R. Slansky, in *Supergravity*, Proceedings of the Workshop, Stony Brook, New York, 1979, edited by P. van Nieuwenhuizen and D. Freedman (North-Holland, Amsterdam, 1979), p. 315; T. Yanagida, in *Proceedings of the Workshop on Unified Theory and the Baryon Number in the Universe*, Tsukuba, Ibaraki, Japan, 1979, edited by O. Sawada and A. Sugamoto [KEK Report No. 79-18, Tsukuba, Japan, 1979 (unpublished)], p. 95.

[3] L. Wolfenstein, Phys. Rev. D **17**, 2369 (1978); S. P. Mikheyev and A. Yu. Smirnov, Yad. Fiz. **42**, 1441 (1985) [Sov. J. Nucl. Phys. **42**, 913 (1986)].

[4] J. N. Bahcall, *Neutrino Astrophysics* (Cambridge University Press, Cambridge, England, 1989).

[5] S. P. Mikheyev and A. Yu. Smirnov, Phys. Lett. B **200**, 560 (1988).

[6] X. Shi and D. N. Schramm, Phys. Lett. B **283**, 305 (1992;); X. Shi, D. N. Schramm, and J. N. Bahcall, Phys. Rev. Lett. **69**, 717 (1992).

[7] D. Harley, T. K. Kuo, and J. Pantaleone, Phys. Rev. D **47**, 4059 (1993).

[8] A. S. Joshipura and P. I. Krastev, Phys. Rev. D **50**, 3484 (1994).

[9] E. Ma and J. Pantaleone, Phys. Rev. D **52**, 3673 (1995).

[10] G. L. Fogli, E. Lisi, and D. Montanino, Phys. Rev. D **49**, 3626 (1994).

[11] G. L. Fogli, E. Lisi, and D. Montanino, in the *Proceedings of the 6th International Workshop on Neutrino Telescopes*, Venice, Italy, 1994, edited by M. Baldo Ceolin (University of Padova, Italy, 1994), p. 419.

[12] G. L. Fogli, E. Lisi, and D. Montanino, Astropart. Phys. **4**, 177 (1995).

[13] G. L. Fogli, E. Lisi, and G. Scioscia, Phys. Rev. D **52**, 5334 (1995).

[14] G. L. Fogli and E. Lisi, Phys. Rev. D **52**, 2755 (1995).

[15] R. Davis, Prog. Part. Nucl. Phys. **32**, 13 (1994); B. T. Cleveland *et al.*, in *Neutrino '94*, Proceedings of the 16th International Conference on Neutrino Physics and Astrophysics, Eilat, Israel, edited by A. Dar, G. Eilam, and M. Gronau [Nucl. Phys. B (Proc. Suppl.) **31**, 47 (1995)].

[16] GALLEX Collaboration, P. Anselmann *et al.*, Phys. Lett. B **357**, 237 (1995).

[17] SAGE Collaboration, J. S. Nico *et al.*, in *ICHEP '94*, Proceedings of the 27th International Conference on High Energy Physics, Glasgow, Scotland, edited by P. J. Bussey and I. Knowles (Institute of Physics Publishing, Bristol, 1995), Vol. II, p. 965; J. N. Abdurashitov *et al.*, Phys. Lett. B **328**, 234 (1994).

[18] Kamiokande Collaboration, Y. Suzuki *et al.*, in *Neutrino '94* [15], p. 54; K. S. Hirata *et al.*, Phys. Rev. D **44**, 2241 (1991); *ibid.* **45**, 2170(E) (1992).

[19] J. N. Bahcall and M. H. Pinsonneault, Rev. Mod. Phys. **67**, 781 (1995).

[20] G. L. Fogli and E. Lisi, Astropart. Phys. **3**, 185 (1995).

[21] G. L. Fogli and E. Lisi, Astropart. Phys. **2**, 91 (1994).

[22] N. Hata and P. Langacker, Phys. Rev. D **50**, 632 (1994).

[23] E. Gates, M. Krauss, and M. White, Phys. Rev. D **51**, 2631 (1995).

[24] Y. Takeuchi, Ph.D. thesis, Tokyo Institute of Technology, 1995.

[25] S. M. Bilenky and S. T. Petcov, Rev. Mod. Phys. **59**, 671 (1987).

[26] S. P. Mikheyev and A. Yu. Smirnov, Prog. Part. Nucl. Phys. **23**, 41 (1989).

[27] T. K. Kuo and J. Pantaleone, Rev. Mod. Phys. **61**, 937 (1989).

[28] W. C. Haxton, Annu. Rev. Astron. Astrophys. **33**, 459 (1995).

[29] S. P. Rosen and J. M. Gelb, Phys. Rev. D **34**, 969 (1986).

[30] A. J. Baltz and J. Weneser, Phys. Rev. D **35**, 528 (1987); **37**, 3364 (1988).

[31] S. Hiroi, H. Sakuma, T. Yanagida, and M. Yoshimura, Phys. Lett. B **189**, 403 (1987).

[32] D. L. Anderson, *Theory of the Earth* (Blackwell, Boston, 1989).

[33] S. M. Bilenky and C. Giunti, Astropart. Phys. **2**, 353 (1994).

[34] G. Fiorentini, M. Lissia, G. Mezzorani, M. Moretti, and D. Vignaud, Phys. Rev. D **49**, 6298 (1994); V. Berezinsky, G. Fiorentini, and M. Lissia, Phys. Lett. B **341**, 38 (1994).

[35] P. I. Krastev and A. Yu. Smirnov, Phys. Lett. B **338**, 282 (1994).

[36] P. I. Krastev and S. T. Petcov, Nucl. Phys. **B449**, 605 (1995).

[37] N. Hata and P. Langacker, Phys. Rev. D **52**, 420 (1995).

[38] J. N. Bahcall and P. I. Krastev, Phys. Rev. D **53**, 4211 (1996).

[39] Particle Data Group, L. Montanet *et al.*, Phys. Rev. D **50**, 1173 (1994).

[40] T. K. Kuo and J. Pantaleone, Phys. Rev. Lett. **57**, 1805 (1986).

[41] S. Toshev, Phys. Lett. B **185**, 177 (1987;); S. T. Petcov and S. Toshev, *ibid.* **187**, 120 (1987); S. T. Petcov, *ibid.* **214**, 259 (1988).

[42] C. W. Kim and W. K. Sze, Phys. Rev. D **35**, 1404 (1987); H. W. Zaglauer and K. H. Schwarzer, Z. Phys. C **40**, 273 (1988); A. Joshipura and M. V. N. Murthy, Phys. Rev. D **37**, 1374 (1988).

[43] H. Minakata, Phys. Lett. B **356**, 61 (1995).

[44] S. M. Bilenky, A. Bottino, C. Giunti, and C. W. Kim, Phys. Lett. B **356**, 273 (1995).

[45] S. Parke, Phys. Rev. Lett. **57**, 1275 (1986).

[46] W. C. Haxton, Phys. Rev. Lett. **57**, 1271 (1986); Phys. Rev. D **35**, 2352 (1987); D. Nötzold, *ibid.* **36**, 1625 (1987); P. Pizzochero, *ibid.* **36**, 2293 (1987); T. Kaneko, Prog. Theor. Phys. **78**, 532 (1987); M. Ito, T. Kaneko, and M. Nakagawa, *ibid.* **79**, 13 (1988); S. T. Petcov, Phys. Lett. B **191**, 299 (1987); S. Toshev, *ibid.* **196**, 170 (1987); **198**, 551 (1987).

[47] L. D. Landau, Phys. Z. Sowjetunion **2**, 46 (1932); C. Zener, Proc. R. Soc. London **A137**, 696 (1932); E. C. G. Stueckelberg, Helv. Phys. Acta **5**, 369 (1932).

[48] S. T. Petcov, Phys. Lett. B **200**, 373 (1988); in *Weak Interactions and Neutrinos,* Proceedings of the Workshop, Ginosar, Israel, 1989, edited by P. Singer and B. Gad Eilam [Nucl. Phys. B (Proc. Suppl.) **13**, 572 (1990)].

[49] P. I. Krastev and S. T. Petcov, Phys. Lett. B **207**, 64 (1988); **214**, 661(E) (1988).

[50] M. Bruggen, W. C. Haxton, and Y.-Z. Qian, Phys. Rev. D **51**, 4028 (1995).

[51] B. Pontecorvo, Zh. Eksp. Teor. Fiz. **53**, 1717 (1967) [Sov. Phys. JETP **26**, 984 (1968)]; S. L. Glashow and L. M. Krauss, Phys. Lett. B **190**, 199 (1987); P. I. Krastev and S. T. Petcov, Phys. Rev. D **53**, 1665 (1996).

[52] P. F. Harrison, D. H. Perkins, and W. G. Scott, Phys. Lett. B **374**, 111 (1996); S. M. Bilenky and C. Giunti, Torino University Report No. DFTT-3-96, hep-ph/9601389 (unpublished); S. M. Bilenky, C. Giunti, and C. W. Kim, Torino University Report No. DFTT-6-96, hep-ph/9602383 (unpublished).

[53] Y. Totsuka *et al.*, ''SuperKamiokande,'' University of Tokyo (ICRR) Report No. ICRR-227-90-20, 1990 (unpublished).

[54] SNO Collaboration, G. T. Ewan *et al.*, ''Sudbury Neutrino Observatory Proposal,'' Report No. SNO-87-12, 1987 (unpublished); ''Scientific and Technical Description of the Mark II SNO Detector,'' Queen's University Report No. SNO-89-15, 1989 (unpublished).

[55] ICARUS Collaboration, ''ICARUS II, a second-generation proton-decay experiment and neutrino observatory at the Gran Sasso Laboratory,'' Laboratori Nazionali del Gran Sasso (LNGS, Italy) Report No. 94/99, Vol. I and II (unpublished); LNGS Report No. 95/10 (unpublished).

[56] C. Giunti, C. W. Kim, and J. D. Kim, Phys. Lett. B **352**, 357 (1995); P. F. Harrison, D. H. Perkins, and W. G. Scott, *ibid.* **349**, 137 (1995); R. N. Mohapatra and S. Nussinov, *ibid.* **346**, 75 (1995).

[57] M. Narayan, M. V. N. Murthy, G. Rajasekaran, and S. Uma Sankar, Phys. Rev. D **53**, 2809 (1996).